Rotating colloids in rotating magnetic fields: Dipolar relaxation and hydrodynamic coupling

Anna C. H. Coughlan and Michael A. Bevan*
Chemical & Biomolecular Engineering, Johns Hopkins University, Baltimore, Maryland 21218, USA
(Received 5 July 2016; revised manuscript received 16 August 2016; published 26 October 2016)

Video microscopy (VM) experiments and Brownian dynamics (BD) simulations were used to measure and model superparamagnetic colloidal particles in rotating magnetic fields for interaction energies on the order of the thermal energy, kT. Results from experiments and simulations were compared for isolated particle rotation, particle rotation within doublets, doublet rotation, and separation within doublets vs field rotation frequency. Agreement between VM and BD results was obtained at all frequencies and amplitudes only by including exact two-body hydrodynamic interactions and relevant relaxation times of magnetic dipoles. Frequency-dependent particle forces and torques cause doublets to rotate at low frequencies via dipolar interactions and at high frequencies via hydrodynamic translation-rotation coupling. By matching measurements and simulations for a range of conditions, our findings unambiguously demonstrate the quantitative forms of dipolar and hydrodynamic interactions necessary to capture nonequilibrium, steady-state dynamics of Brownian colloids in magnetic fields.

DOI: 10.1103/PhysRevE.94.042613

I. INTRODUCTION

The dynamics of magnetic colloidal particles in time-dependent magnetic fields is relevant to many applications such as measuring biomolecular interactions [1,2], developing microfluidic devices [3,4], tuning magnetorheological suspensions [5], and increasingly, colloidal assembly [6–10]. For example, magnetic dipolar colloidal chains can be used to tune suspension rheological properties by forming, bending, breaking, translating, and rotating in dynamic fields [11–14]. Microstructures of dipolar colloidal particles can be manipulated in external fields to form chains, clusters, crystals, and many other configurations [15–17]. Controlling colloidal interactions in rotating fields is becoming a promising approach to manipulate two-dimensional colloidal assembly [6–9] as well as three-dimensional microstructures [17]. Rotating fields, when combined with field gradients, can also transport, disperse, and order colloidal particles [18].

In applications involving magnetic colloids, it is important to understand how single dipoles interact with dynamic magnetic fields in balance with hydrodynamic drag. Superparamagnetic micron-sized particles have induced dipoles that display a range of relaxation times based on the ensemble response of individual magnetic domains (due to many magnetic nanoparticles dispersed within each micron-sized colloidal particle). Practically, for a given field frequency, a separation of relaxation times allows net dipoles to be considered as the sum of two contributions: (1) Néel dipoles that appear to be instantaneous as a result of their relatively fast relaxation via stochastic reorientation within magnetic domains, and (2) Brownian dipoles that appear to be permanent as a result of their slow relaxation relative to the stochastic rotation of the colloidal particle [19,20]. Both of these dipoles contribute to frequency-dependent dipole-field torques in rotating fields while viscous forces oppose rotation. Previous work has shown the fast Néel relaxation dominates the ensemble dipole [21].

In addition to single particle interactions, two (or more) particles have been shown to rotate in response to external fields due to particle-particle interactions, including dipole-dipole and hydrodynamic interactions. Dipole-dipole interactions lead to torques on particle doublets (or chains) due to the favorable head-to-tail alignment of dipoles [8,22–24]. Particle-particle interactions also determine whether doublets rotate as rigid bodies or as free rotating particles. For doublets to rotate rigidly, a tangential force between two particles is required (which has been used to study macromolecular and electrostatic interactions [25,26]). Rigidly rotating doublets rotate slower than doublets in which the particles can freely rotate. These results suggest that the dynamics of individual particles within doublets, as well as particle-particle interactions, are crucial to understanding doublet rotation (and vice versa).

Previous research suggests that hydrodynamic interactions and dipole relaxation both affect the frequency dependence of magnetic doublet rotation in rotating fields. It has been observed that doublets rotate at the same frequency as rotating fields up to a critical frequency, after which the rotation rate declines due to viscous drag [8,23,28,29]. These studies showed at frequencies slightly higher than the critical frequency that (1) individual dipoles no longer remain aligned along the line of centers; (2) for freely rotating doublets, the interparticle distance oscillates; and (3) for both rigid and freely rotating doublets, the angular trajectories oscillate about an average steady rotational velocity. At even higher frequencies, where Brownian relaxation cannot occur, larger clusters [9,30] and rigid doublets [31] continue to rotate, which has been suggested to occur via the balance of an out-of-phase dipole and hydrodynamic interactions. Although prior modeling studies of small chains and clusters have considered various aspects relevant to rotating doublets in rotating fields (including hydrodynamic interactions [11–14], translation-rotation coupling [32], and nontrivial Néel relaxation [30,31]), none have included thermal motion, exact hydrodynamics, and dipolar relaxation necessary to quantify both single particles and doublet rotation and relative particle translation vs frequency.

In this work, we investigate superparamagnetic particles in rotating magnetic fields including single particle rotation, doublet rotation, single particle rotation within rotating doublets, and relative particle translation within doublets (see Fig. 1).

*mabevan@jhu.edu

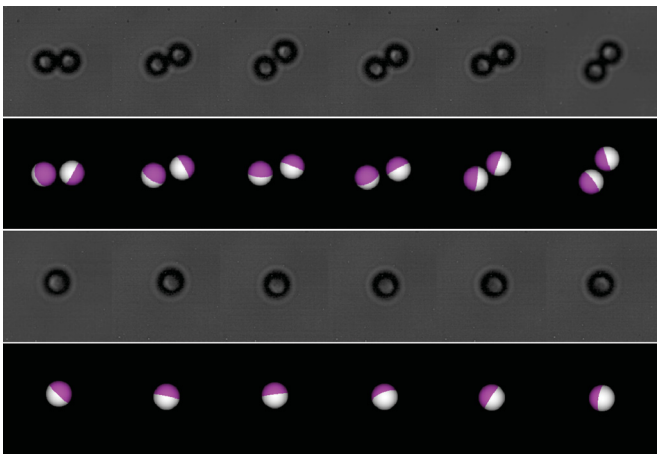

FIG. 1. Single particle and doublet rotation in experimental images and BD simulation renderings (6 G, 0.8 Hz; image time step of 0.167 s) (see Videos S1–S3 in the Supplemental Material (SM) [27]). Experimental images are processed via analysis algorithms described in the Materials and Methods section and depicted in Fig. 4 to provide raw trajectory data that are averaged and filtered via fast Fourier transforms to identify dominant rotational modes in frequency spectra.

Video microscopy (VM) is used to measure the translation and rotation of particles vs field rotation frequency for small field amplitudes that allow for thermal motion to probe kT-scale interactions. Each experiment is simulated using BD simulations that include conservative forces and torques (i.e., the gradients of scalar potential functions), nonconservative forces and torques (i.e., exact pair hydrodynamic interactions between particles including translation-rotation coupling and near field and far field [33]), Brownian motion, and the effects of a distribution of relaxation times. To increase model complexity in a systematic fashion, we first match simulations and experiments for single particles by determining their dipole moments and their relaxation vs field rotation frequency. We then measure and model all rotational and translational modes in doublets vs field frequency. This process provides a unique rigorous model that qualitatively and in most cases quantitatively captures all frequency-dependent interactions and dynamics of superparamagnetic Brownian colloids in rotating magnetic fields.

II. THEORY

A. Equation of motion

The translational and rotational motion of a particle with mass m can be expressed by the Langevin equation as (for coordinates labeled in Fig. 2) [34]

$$m\frac{d\mathbf{u}}{dt} = \mathbf{F}^P + \mathbf{F}^H + \mathbf{F}^B, \tag{1}$$

$$m\frac{d\boldsymbol{\omega}}{dt} = \mathbf{T}^P + \mathbf{T}^H + \mathbf{T}^B, \tag{2}$$

where $\mathbf{u}$ and $\boldsymbol{\omega}$ are translational and angular velocity vectors, and $\mathbf{F}$ and $\mathbf{T}$ are force and torque vectors. Superscripts in Eqs. (1) and (2) denote contributions from P, conservative forces on particles due to the gradient of a scalar potential field;

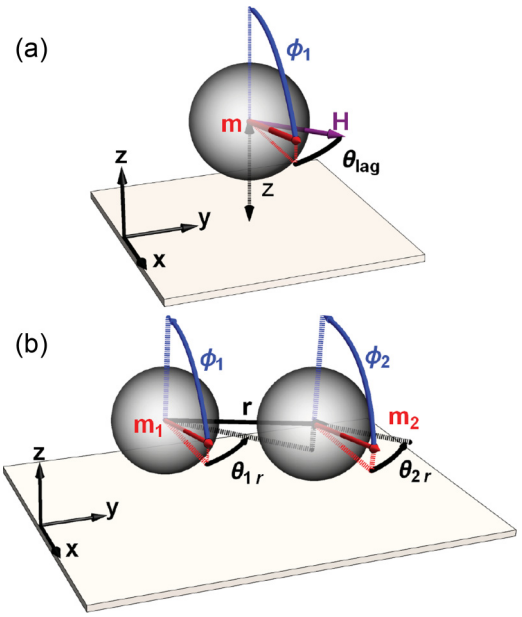

FIG. 2. Schematics showing (a) a dipole $\mathbf{m}$, defined in Eq. (20), and its phase lag in the x-y plane with respect to a field $\mathbf{H}$, which produces a torque on the particle as expressed in Eq. (37); and (b) the relevant angles and vectors of a doublet system, including dipole polar and azimuthal angles with respect to the particle-particle vector $\mathbf{r}$ in the x-y plane, used in the dipole-dipole potential, Eq. (16) (note k has been dropped to generalize the schematic).

H, nonconservative forces due to hydrodynamic interactions that couple translation and rotation between particles; and B, random thermal forces and torques due to Brownian motion.

Particle position vs time is modeled by solving the Langevin equation for position. A new position $\mathbf{r}_l$ where l coordinates correspond to translation only (i.e., $l \leqslant 3N$) is calculated as

$$\mathbf{r}_l = \mathbf{r}_l^0 + \sum_j \frac{\partial \mathbf{D}_{lj}^0}{\partial \mathbf{r}_j}\Delta t + \sum_{j,j\leqslant 3N} \frac{\mathbf{D}_{lj}^0\left(\mathbf{F}_j^{P,0} + \mathbf{F}_j^B\right)}{kT}\Delta t + \sum_{j,j>3N} \frac{\mathbf{D}_{lj}^0\left(\mathbf{T}_j^{P,0} + \mathbf{T}_j^B\right)}{kT}\Delta t, \tag{3}$$

where $\mathbf{F}_j^{P,0}$ and $\mathbf{T}_j^{P,0}$, $\mathrm{T}_j^{P,0}$ are the force and torque vectors at the start of each step; and $\mathbf{F}_j^B$ and $\mathbf{T}_j^B$ are the random force and torque vectors. Brownian dynamics of the angular displacement of a particle has been derived in a similar manner [34]. The orientation of the particle main axis is calculated from unit vector $\mathbf{n}$ whose displacement is related to the conservative forces and torques as [35]

$$\mathbf{n}_l(t+\Delta t) = \mathbf{n}_l(t) + \left[\sum_{j,j>3N} \frac{\mathbf{D}_{lj}^0}{kT}\left(\mathbf{T}_j^{P,0} + \mathbf{T}_j^B\right) + \sum_{j,j\leqslant 3N} \frac{\mathbf{D}_{lj}^0}{kT}\left(\mathbf{F}_j^{P,0} + \mathbf{F}_j^B\right)\right] \times \mathbf{n}_l(t)\Delta t, \tag{4}$$

where l coordinates correspond to rotation only; i.e., $l > 3N$.

B. Conservative forces and torques

A colloidal particle experiences a net potential energy that includes particle-wall, particle-field, and particle-particle interactions with a nearby particle. The dipoles are distinguished using an index, k, where $k = N,B$ for Néel and Brownian, respectively, as shown,

$$u^{\text{net}}(\theta_{1,k},\theta_{2,k},\phi_{1,k},\phi_{2,k},\mathbf{r},z) = u^{pw}(z) + u^{pf}(\theta_{1,k},\phi_{1,k},z) + u^{pp}(\theta_{1,k},\theta_{2,k},\phi_{1,k},\phi_{2,k},\mathbf{r}), \tag{5}$$

where $\theta_{l,k}$ and $\phi_{l,k}$ are the azimuthal and polar angles of the l particle-centered dipole moment, $\mathbf{r}$ is the 1–2 center-to-center distance, and z is the particle center-to-wall-surface position. Three-dimensional force and torque vectors can be derived from Eq. (5) by taking partial derivatives with respect to a position or angle, keeping all other variables constant. For example, the force along the $\mathbf{r}$ direction and the torque in $\theta_{l,k}$ are given by

$$\mathbf{F}_r{}^P = -\frac{\partial}{\partial r}u^{\text{net}}(\theta_{1,k},\theta_{2,k},\phi_{1,k},\phi_{2,k},\mathbf{r},z), \tag{6}$$

$$\mathbf{T}^P_{\theta_{1,k}} = -\frac{\partial}{\partial \theta_{1,k}}u^{\text{net}}(\theta_{1,k},\theta_{2,k},\phi_{1,k},\phi_{2,k},\mathbf{r},z). \tag{7}$$

C. Particle-wall potential

The only interaction with the particle and the wall is electrostatics [36], given by

$$u^{pw}_{el}(z) = B^{pw}\exp[-\kappa(z-a)], \tag{8}$$

$$B^{pw} = 64\pi\varepsilon_m a\left(\frac{k_BT}{z_ve}\right)^2\tanh\left(\frac{z_ve\varsigma_p}{4k_BT}\right)\tanh\left(\frac{z_ve\varsigma_w}{4k_BT}\right), \tag{9}$$

where a is particle radius, κ^{-1} is Debye length, k_B is Boltzmann's constant, T is the temperature, ε_m is the medium permittivity, e is the charge of an electron, z_v is the electrolyte valence, and ς_p and ς_w are the particle and wall surface potentials.

D. Particle-field potentials

Particle-field interactions include gravitational and dipole-magnetic field mediated potentials given as

$$u^{pf}(\theta_{1,k},\phi_{1,k},z) = u^{pf}_g(z) + u^{pf}_{df}(\theta_{1,k},\phi_{1,k}), \tag{10}$$

such that the gravitational field only depends on z,

$$u^{pf}_g(z) = \tfrac{4}{3}\pi a^3(\rho_p - \rho_m)gz = Gz, \tag{11}$$

where ρ_p and ρ_m are particle and medium densities, and g is acceleration due to gravity. A particle dipole of moment, $\mathbf{m}$, interacts with a magnetic field, $\mathbf{H}$ [37], as given by [see Fig. 2(a)]

$$u^{pf}_{df}(\theta_{1,k},\phi_{1,k}) = -\mathbf{m}\cdot\mu_0\mathbf{H}, \tag{12}$$

where $\mathbf{m}$ can correspond to either a Néel or Brownian dipole (discussed in the following) and μ_0 is the permeability of free space.

E. Particle-particle potentials

Two interacting particles experience a magnetic dipole-dipole potential and an electrostatic double layer repulsion as

$$u^{pp}(\theta_{1r,k},\theta_{2r,k},\phi_{1,k},\phi_{2,k},\phi_r,r) = u^{pp}_{el}(r) + u^{pp}_{dd}(\theta_{1r,k},\theta_{2r,k},\phi_{1,k},\phi_{2,k},\phi_r,r), \tag{13}$$

where angles in the x-y plane relative to the particles' center-to-center vector, $\mathbf{r}$, are denoted as $\theta_{1r,k}$ and $\theta_{2r,k}$; the subscript r indicates the angles are relative to $\mathbf{r}$ [see Fig. 2(b); note k is dropped]. At low ionic strengths, particles do not experience van der Waals attraction and only the electrostatic term from Derjaguin, Landau, Verwey, Overbeek (DLVO) theory needs to be taken into account, which is given by [36]

$$u^{pp}_{el}(r) = B^{pp}\exp[-\kappa(r-2a)], \tag{14}$$

$$B^{pp} = 32\pi\varepsilon_m a\left(\frac{k_BT}{z_ve}\right)^2\tanh\left(\frac{z_ve\varsigma_p}{4k_BT}\right)^2. \tag{15}$$

The magnetic dipole-dipole interaction is given by (expanding the typical vector expression) [37]

$$u^{pp}_{dd}(\theta_{1r,k},\theta_{2r,k},\phi_{1,k},\phi_{2,k},\phi_r,r) = \frac{\mu_o}{4\pi r^3}\sum_{k=N,B}m_{1,k}m_{2,k}\left\{\begin{array}{l}\cos(\theta_{1r,k}-\theta_{2r,k})\sin(\phi_{1,k})\sin(\phi_{2,k})+\cos(\phi_{1,k})\cos(\phi_{2,k})\\ -3[\cos(\theta_{1r,k})\sin(\phi_{1,k})\sin(\phi_r)+\cos(\phi_{1,k})\cos(\phi_r)]\\ \times[\cos(\theta_{2r,k})\sin(\phi_{2,k})\sin(\phi_r)+\cos(\phi_{2,k})\cos(\phi_r)]\end{array}\right\}, \tag{16}$$

where $m_{1,k}$ and $m_{2,k}$ are the magnitudes of the dipole moments on particles 1 and 2, which can correspond to either a Néel or Brownian dipole, which we review in more detail in the following section.

F. Magnetic field and dipoles

The force and torque expressions in the preceding sections require the field vector and dipole moments, which are inputs in the particle-field potential [Eq. (12)] and field mediated particle-particle potential [Eq. (16)]. In the following, we provide more detailed information on the time varying external magnetic field, the magnetic fields of nearby particles, and predicted dipole moments based on material properties. In an applied rotating field, the field vector can be expressed as a function of the intensity H_o and the magnetic permeability μ_o such that $H_o = B_o/\mu_o$, where B_o is the applied field. The field orientation depends on rotation speed, ω_f, as (where $\theta_f = \omega_f t$)

$$\mathbf{H}_o = H_o\cos(\theta_f)\hat{\mathbf{x}} + H_o\sin(\theta_f)\hat{\mathbf{y}}. \tag{17}$$

When two particles are in proximity to each other, the field from a neighboring particle's dipole is added to the total field. The magnetic intensity of a nearby particle is given by [38]

$$\mathbf{H}_p(\mathbf{r}) = \frac{3\hat{\mathbf{r}}(\mathbf{m}\cdot\hat{\mathbf{r}}) - \mathbf{m}}{4\pi r^3}, \tag{18}$$

and the total external field in Eq. (12) is the sum of the applied and local dipolar fields given as

$$\mathbf{H} = \mathbf{H}_o + \mathbf{H}_p(\mathbf{r}). \tag{19}$$

When a magnetic dipole moment $\mathbf{m}$ is induced by an external magnetic field (for superparamagnetism [37]), its value is given by

$$\mathbf{m} = \frac{4\pi a^3 \chi(\omega_f)\mathbf{H}}{3}, \tag{20}$$

where $\chi(\omega_f)$ is the dynamic susceptibility, which is a function of the static susceptibility and dipole relaxation times. The dipole in Eq. (20) can be used to compute the dipole-field interaction potential in Eq. (12). Practically, the Brownian dipole is modeled with a fixed magnitude. By combining Eqs. (18)–(20), the Néel dipole on one particle, $\mathbf{m}_{1,N}$, induced by both an applied external field and the Néel, $\mathbf{m}_{2,N}$, and Brownian, $\mathbf{m}_{2,B}$, dipoles of a second adjacent particle is given by

$$\mathbf{m}_{1,N} = \frac{4}{3}\pi a^3 \chi_N(\omega_f)\left[\mathbf{H}_o + \frac{3\hat{\mathbf{r}}(\mathbf{m}_{2,N}\cdot\hat{\mathbf{r}}) - \mathbf{m}_{2,N}}{4\pi r^3} + \frac{3\hat{\mathbf{r}}(\mathbf{m}_{2,B}\cdot\hat{\mathbf{r}}) - \mathbf{m}_{2,B}}{4\pi r^3}\right], \tag{21}$$

where $\chi_N(\omega_f)$ is the dynamic susceptibility corresponding to the Néel dipole only. The magnitudes of the Néel dipoles on particles 1 and 2 for use in the dipole-dipole potential in Eq. (16) are obtained by (1) assuming the dipoles are equal in magnitude and direction (i.e., $\mathbf{m}_{1,N} = \mathbf{m}_{2,N}, \mathbf{m}_{1,B} = \mathbf{m}_{2,B}$) on the right- and left-hand sides of Eq. (21), (2) algebraically solving for either $\mathbf{m}_{1,N}$ or $\mathbf{m}_{2,N}$, and (3) taking the magnitude of the dipole vector to obtain m_1 and m_2. The inaccuracy due to assuming $\mathbf{m}_{1,B} = \mathbf{m}_{2,B}$ (in this equation only) is negligible when the permanent dipoles are much smaller than the instantaneous dipoles.

G. Particle susceptibility

The effective static susceptibility, $\chi_o(H)$, for a spherical particle is defined as a function of the static susceptibility, $\chi(H)$, as [37]

$$\chi_o(H) = \chi(H)[1 + (\chi(H)/3)]^{-1}. \tag{22}$$

The dynamic susceptibility as a function of the fractional contributions of the Néel and Brownian dipoles, f_N and f_B, and their associated relaxation times, τ_N and τ_B, is given by

$$\chi(\omega_f) = \chi_N(\omega_f) + \chi_B(\omega_f), \tag{23}$$

$$\chi(\omega_f) = \chi_o\left[\frac{f_N}{1 + (i\omega_f\tau_N)^{1-\alpha}} + \frac{f_B}{1 + i\omega_f\tau_B}\right], \tag{24}$$

where α determines the Néel relaxation time distribution width [39,40]. If some of the individual Néel dipoles have relaxation times on the order of the field rotation rate, they cannot overcome the energy barrier to reorient with the field [41,42]. As a result, the Néel dipole in a rotating field has in-phase, $\chi'_N(\omega_f)$, and out-of-phase, $\chi''_N(\omega_f)$ components of the susceptibility as [20]

$$\chi_N(\omega_f) = \frac{f_N\chi_o}{1 + (i\omega_f\tau_N)^{1-\alpha}} = \chi'_N(\omega_f) - i\chi''_N(\omega_f). \tag{25}$$

The Néel phase lag is defined as

$$\theta_{\mathrm{lag},N}(\omega_f) = \arctan\left[\frac{\chi''_N(\omega_f)}{\chi'_N(\omega_f)}\right], \tag{26}$$

and components can be modeled as [39]

$$\chi''_N(\omega_f) = \frac{f_N\chi_o(\omega_f\tau_N)^{1-\alpha}\cos\left(\frac{1}{2}\pi\alpha\right)}{1 + 2(\omega_f\tau_N)^{1-\alpha}\sin\left(\frac{1}{2}\pi\alpha\right) + (\omega_f\tau_N)^{2(1-\alpha)}}, \tag{27}$$

$$\chi'_N(\omega_f) = \frac{f_N\chi_o\left[1 + (\omega_f\tau_N)^{1-\alpha}\sin\left(\frac{1}{2}\pi\alpha\right)\right]}{1 + 2(\omega_f\tau_N)^{1-\alpha}\sin\left(\frac{1}{2}\pi\alpha\right) + (\omega_f\tau_N)^{2(1-\alpha)}}. \tag{28}$$

H. Hydrodynamic forces and torques

Hydrodynamic forces and torques oppose translational and rotational motion of the particle. For low-Reynolds number dynamics, translational and angular velocities of particles can be directly related to the forces and torques by a mobility matrix, $\mathbf{M}$, given as

$$\begin{pmatrix}\mathbf{u_1}\\ \mathbf{u_2}\\ \boldsymbol{\omega_1}\\ \boldsymbol{\omega_2}\end{pmatrix} = \mathbf{M}\begin{pmatrix}\mathbf{F}_1\\ \mathbf{F}_2\\ \mathbf{T}_1\\ \mathbf{T}_2\end{pmatrix}, \tag{29}$$

$$\mathbf{M} = \begin{pmatrix}\mathbf{a_{11}} & \mathbf{a_{12}} & \tilde{\mathbf{b}}_{\mathbf{11}} & \tilde{\mathbf{b}}_{\mathbf{12}}\\ \mathbf{a_{21}} & \mathbf{a_{22}} & \tilde{\mathbf{b}}_{\mathbf{21}} & \tilde{\mathbf{b}}_{\mathbf{22}}\\ \mathbf{b_{11}} & \mathbf{b_{12}} & \mathbf{c_{11}} & \mathbf{c_{12}}\\ \mathbf{b_{21}} & \mathbf{b_{22}} & \mathbf{c_{21}} & \mathbf{c_{22}}\end{pmatrix}, \tag{30}$$

where $\mathbf{M}$ is the mobility matrix containing near-field and far-field terms, obtained for two particles using twin multipole expansions [33]. When expanded, the mobility matrix has $6N\times6N$ terms. Here, $N = 2$ so that the mobility matrix $\mathbf{M}$ is 12×12. If the particles are infinitely far from each other, only diagonal terms are nonzero and for spheres, $a_{ii} = 1/6\pi\eta a$ and $c_{ii} = 1/8\pi\eta a^3$. The mobility matrix is related to the resistance matrix, $\mathbf{R}$, by

$$\mathbf{MR} = \mathbf{I}$$

$$\begin{pmatrix}\mathbf{a_{11}} & \mathbf{a_{12}} & \tilde{\mathbf{b}}_{\mathbf{11}} & \tilde{\mathbf{b}}_{\mathbf{12}}\\ \mathbf{a_{21}} & \mathbf{a_{22}} & \tilde{\mathbf{b}}_{\mathbf{21}} & \tilde{\mathbf{b}}_{\mathbf{22}}\\ \mathbf{b_{11}} & \mathbf{b_{12}} & \mathbf{c_{11}} & \mathbf{c_{12}}\\ \mathbf{b_{21}} & \mathbf{b_{22}} & \mathbf{c_{21}} & \mathbf{c_{22}}\end{pmatrix}\begin{pmatrix}\mathbf{A_{11}} & \mathbf{A_{12}} & \tilde{\mathbf{B}}_{\mathbf{11}} & \tilde{\mathbf{B}}_{\mathbf{12}}\\ \mathbf{A_{21}} & \mathbf{A_{22}} & \tilde{\mathbf{B}}_{\mathbf{21}} & \tilde{\mathbf{B}}_{\mathbf{22}}\\ \mathbf{B_{11}} & \mathbf{B_{12}} & \mathbf{C_{11}} & \mathbf{C_{12}}\\ \mathbf{B_{21}} & \mathbf{B_{22}} & \mathbf{C_{21}} & \mathbf{C_{22}}\end{pmatrix} = \begin{pmatrix}1 & 0 & 0 & 0\\ 0 & 1 & 0 & 0\\ 0 & 0 & 1 & 0\\ 0 & 0 & 0 & 1\end{pmatrix}. \tag{31}$$

The elements in **R** are dependent upon the relative distances and orientations of particles as given by expressions using the notation of the original reference [33],

$$\begin{aligned} A_{ij}^{\alpha\beta} &= X_{\alpha\beta}^{A} e_i e_j + Y_{\alpha\beta}^{A}(\delta_{ij} - e_i e_j), \\ B_{ij}^{\alpha\beta} &= \tilde{B}_{ji}^{\beta\alpha} = Y_{\alpha\beta}^{B}\varepsilon_{ijk} e_k, \\ C_{ij}^{\alpha\beta} &= X_{\alpha\beta}^{C} e_i e_j + Y_{\alpha\beta}^{C}(\delta_{ij} - e_i e_j), \end{aligned} \tag{32}$$

where the terms on the right-hand side correspond to Jeffrey and Onishi's resistance functions defined at "arbitrary separations" (including recently reported corrections [43]), α,β correspond to particle number, and $\boldsymbol{e} = \mathbf{r}/r$ such that $e_i e_j$ and $\delta_{ij} - e_i e_j$ indicate parallel and perpendicular to the line of particle centers, respectively.

I. Brownian forces and torques

The Brownian force and torque can be combined into one vector $\mathbf{S}^B$ as

$$\mathbf{S}^B = \begin{pmatrix} \mathbf{F}^B \\ \mathbf{T}^B \end{pmatrix}, \tag{33}$$

which follows a Gaussian distribution with a mean of zero and variance given by

$$\left\langle \mathbf{S}_i^B(0)\mathbf{S}_j^B(t)\right\rangle = 2(kT)^2\mathbf{D}_{ij}^{-1}\delta(t), \tag{34}$$

where in practice $\mathbf{S}^B$ is computed from a vector of normal deviates weighted by a Cholesky decomposition of the resistance matrix, **R** [34].

J. Particle and doublet rotation

The angular velocity of a particle in a rotating magnetic field can be calculated by balancing the viscous torque, $\mathbf{T}^{H,R}$, against the dipole-magnetic field torque, $\mathbf{T}_{df}^{P}$, as

$$\mathbf{T}_{df}^{P} = -\mathbf{T}^{H,R}. \tag{35}$$

The gradient of the dipole-field potential [Eq. (12)] with respect to orientation gives the torque on the dipole moment of a particle, which is the sum of the torques due to the Néel and Brownian dipolar contributions given as

$$\mathbf{T}_{df}^{P} = \sum_{k=N,B} \mathbf{m}_k \times \mu_o \mathbf{H}. \tag{36}$$

In a field in the x-y plane, Eq. (36) depends on the angle of the dipole in the x-y plane, $\theta_{l,k}$, and with respect to the z axis $\phi_{l,k}$ [see Fig. 2(a)] as given by

$$T_{df,z}^{P} = \sum_{k=N,B} m_k \mu_o H_o \sin\left(\theta_f - \theta_{1,k}\right)\sin\left(\phi_{1,k}\right), \tag{37}$$

and $\theta_{\mathrm{lag},k} = \theta_f - \theta_{1,k}$ is defined as the phase lag of either the Néel dipole [from Eq. (26)] or Brownian dipole (determined directly from the particle main axis).

For isolated particles, the particle is also rotating around the axis perpendicular to the wall, leading to a negligible wall hydrodynamic correction [44], and negligible motion with respect to the polar axis is assumed. As such, the hydrodynamic drag is approximated as

$$T_z^{H,R} = \omega_p 8\pi\eta a^3. \tag{38}$$

For the Néel dipole, only the out-of-phase component contributes to the torque; therefore the velocity can be written as [using Eq. (20) for the Néel out-of-phase dipole]

$$\omega_p = \frac{m_B \mu_o H_o \sin\left(\theta_f - \theta_{1,B}\right) + \frac{4}{3}\pi a^3 \chi''_N(\omega_f)\mu_o H_o^2}{8\pi\eta a^3}. \tag{39}$$

The critical frequency is the frequency at which the particle experiences a maximum dipole-field torque. If the critical frequency is less than the field frequency, the angle between the particle and the field gradually increases. When that angle reaches 180°, the particle experiences backwards rotation until it is once again aligned with the field. The frequency of one such forwards-backwards oscillation for single particles can be inferred from a previous model for rigid doublet rotation [22]. When this model is applied to a single particle, the oscillation frequency, ω_{osc}, relates to single particle critical frequency, ω_{crit}, and field frequency as

$$\omega_{\mathrm{osc}} = \omega_{\mathrm{crit}}\sqrt{\left(\frac{\omega_f}{\omega_{\mathrm{crit}}}\right)^2 - 1}. \tag{40}$$

During each oscillation for single particles, the particle axis angular displacement is −360° with respect to the field. In this regime, the average frequency of particle rotation is the difference in the field frequency and the frequency of one oscillation cycle given by

$$\bar{\omega} = \omega_f - \omega_{\mathrm{osc}}. \tag{41}$$

Similar to the single particle analysis, a critical frequency exists for a rotating rigid doublet. The oscillation frequency has the same form as Eq. (40) but considers the weighted contribution from both Néel and Brownian dipoles as given by

$$\frac{\omega_{d,\mathrm{osc}}}{2} = \omega_{d,\mathrm{crit}}\sqrt{\left(\frac{\sum\limits_{k=N,B} m_k\omega_k}{\sum\limits_{k=N,B} m_k}\Big/\omega_{d,crit}\right)^2 - 1}, \tag{42}$$

where $\omega_{d,crit}$ and $\omega_{d,\mathrm{osc}}$ are the critical and oscillation frequencies of the doublet vector **r**. In one cycle of forwards-backwards rotation, the doublet angular displacement is −180° with respect to the average dipole trajectory. The average frequency of rotation in this regime is the difference in the overall dipole rotation and half of one doublet-oscillation cycle given by

$$\bar{\omega}_d = \left[\frac{\sum\limits_{k=N,B} m_k\omega_k}{\sum\limits_{k=N,B} m_k}\right] - \frac{\omega_{d,\mathrm{osc}}}{2}. \tag{43}$$

III. MATERIALS AND METHODS

A. Particles and surfaces

M-270 carboxylic acid-coated microparticles composed of iron oxide nanoparticles embedded in a polystyrene matrix with nominal diameter 2.8 μm were used as received (Dynabeads, Life Technologies). To visualize particle orientation, a nonmagnetic film was coated on one hemisphere to make "optical Janus" particles (Fig. 1). The particles as received were dried as a monolayer on a glass slide. The slides with

the half-exposed dried particles were coated using an E-beam evaporator by first depositing a 15-nm thin film of Cr to aid the adhesion of Au, followed by a 35-nm Au film, and finally a 30-nm SiO_2 film. The microscope slides were sonicated in de-ionized (DI) water to remove the coated particles from the surface and the solution was centrifuged to collect the particles.

Experiments were conducted on glass cover slips (Gold Seal, Corning) for 100× objectives or regular glass slides (Fisher Scientific) for 40× objectives. Cover slips or slides were sonicated in acetone (Sigma-Aldrich Company) and then isopropanol (Sigma-Aldrich Company), and soaked in Nochromix (Godax Laboratories) for 1–24 h, rinsed in de-ionized water, sonicated in 0.1*M* KOH for 35 min to charge the surface, rinsed with de-ionized water, and dried with nitrogen gas. Sample cells containing dilute particles in 0.1m*M* NaCl were prepared by dispensing the dispersion into Viton O-rings (McMaster-Carr) coated with vacuum grease on cover slips or slides and sealed using epoxy quick set glue (Loctite) and a top cover slip.

B. Microscopy and magnetic field apparatus

For rotating doublet and single particle magnetophoresis experiments, a 40× objective (Nikon) was used to monitor particles. For single particle and particle rotation in doublet experiments, a 100× oil objective (Nikon) was used to detect orientation of "optical Janus" particles. For all experiments, a Photron PCI-512 camera was used to record video at 60 or 120 frames per second (fps) of the field of view of the microscope. Cover slips or slides with the colloidal particles were placed on a stage in the center of a magnetic quadrupole setup, which has been described elsewhere [45]. Briefly, two sets of four solenoids are arranged in a quadrupole (see Fig. 3) and solenoids receive a current that is 90° out of phase with the preceding solenoid to produce a constantly rotating field with uniform magnitude. In a second operating mode, a differential current through opposing solenoids creates a controllable field gradient along a single axis. A uniform 5 G/mm gradient was applied for magnetophoresis experiments.

Videos were analyzed using particle tracking codes written in FORTRAN for doublet rotation or in MATLAB for particle rotation using algorithms similar to others reported in the literature [19,46–48]. For particle angular orientation images, we apply the bandpass filter bpass.m (adapted for MATLAB from the original particle tracking codes [49]) that enhances the contrast between the gold particle patch, the rest of the particle, and the background. We then use the MATLAB built-in function bwboundaries to identify the boundaries of our particles and the patch by their higher intensities relative to the rest of the image. The coordinate of the patch is determined by weighting the intensities of all pixels within the patch. For single particles, the center of the particle is the average position of the boundary pixels. For particles within doublets, two circles are fit to the doublet outline to find the centers of the particles. Lastly, the orientation is calculated based on the angle of the patch with respect to the centers of the particles. Figure 4 shows experimental images before and after the analysis is applied for single particles and particles within doublets.

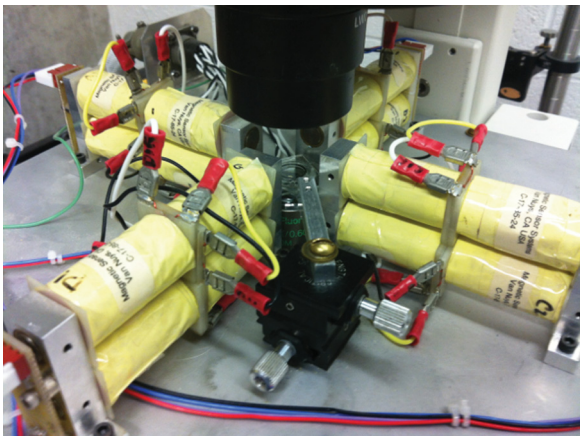

FIG. 3. Image of the magnetic quadrupole apparatus, showing the two sets of four solenoids.

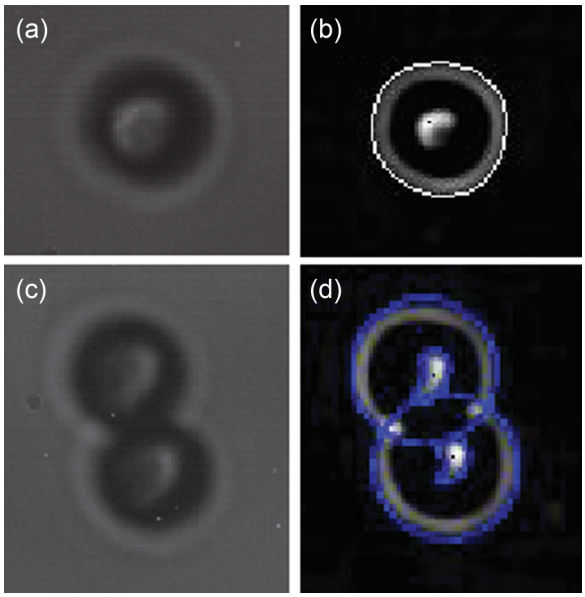

FIG. 4. (a) Experimental image of a single particle with a gold patch, and (b) the corresponding image obtained from increasing the contrast, identifying the outline of the particle and the patch, and calculating the location of the patch, marked with a black dot. (c) An experimental image of two particles within a doublet, both with gold patches, and (d) the corresponding image after analysis, showing in blue the circles fit to the outlines of the particles, the borders of the patches, and the locations of the patches marked with black dots.

C. Particle characterization

Single particle drift in a field gradient, or magnetophoresis, can be used to calculate the static susceptibility as a function of field intensity in the case where the intensity negligibly changes in the field of view [50]. Static susceptibility values (for brevity here and throughout, the effective static susceptibility is referred to as the static susceptibility) calculated from magnetophoresis experiments are shown in Table I. Further details on the measurements are in the Appendix.

The dynamic susceptibility due to the Néel dipole [Eqs. (25)–(28)] was determined by two independent methods: particle property measurement system (PPMS) measurements

TABLE I. Parameters used in the BD simulations.

Parameter	Value	Equation
$-\varsigma_p$ (mV),[a] $-\varsigma_w$ (mV)	50	(9), (15)
a (nm)[b]	1400	(8), (9), (11), (14), (15), (21)
κ^{-1} (nm)	30.3	(8), (14)
χ_o at 6 G[c]	1.46	(24), (25), (27), (28)
χ_o at 10 G[c]	1.33	(24), (25), (27), (28)
α[d]	0.87	(24),(25),(27),(28)
τ_N (s)[d]	2.5×10^{-9}	(24), (25), (27), (28)
m_B (10^{-16} A m^2)[e]	3.0	(12), (16), (21)
f_B at 6 G (%)[f]	3.75	(24), (25)
f_B at 10 G (%)[f]	2.5	(24), (25)
f_N at 6 G (%)[f]	96.25	(24), (25)
f_N at 10 G (%)[f]	97.5	(24), (25)

[a]Reference [8].
[b]Reported by the manufacturer.
[c]Fit to magnetophoresis experiments.
[d]Fit to both PPMS measurements and torque balance experiments.
[e]Fit to single particle critical frequency measurements.
[f]Calculated using m_B and the total dipole [plug in χ_o in Eq. (20)].

and single particle rotation at high frequencies [when the Brownian dipole does not contribute to rotation in Eq. (39)]. Phase lag and the in-phase and out-of-phase components at different magnetic field frequencies were measured using a PPMS (Quantum Design). The magnetic microparticles were characterized either as a powder or in a dried agar matrix. For the powder, the microparticles were dried on a glass slide and scraped off. For the agar matrix, agar powder (Type I, Sigma-Aldrich Company) was heated until dissolved in DI water. Colloids were directly added to the solution and sonicated. The dispersion was then poured onto a Petri dish and left overnight to harden. Prior to measurement, the agar gel was vacuum dried. Frequencies ranged from the minimum of 10 Hz to 200 Hz at a constant field of 10 G and an oscillating field of 6 G. Equations (26)–(28) were used to fit the PPMS measurements for unknowns α and τ_N [note χ_o and f_N cancel in Eq. (26)], assuming they do not change in this field range. In the second method, we conducted a torque balance of single particle rotation at 10, 50, and 100 Hz, each at 6 and 10 G, and fit $\chi_N''(\omega_f)$ [Eq. (27)] via adjustable parameters α and τ_N, given χ_o and an estimate of f_N (which was verified via an iterative method to simultaneously fit the Néel dipole measurements and the Brownian dipole, described below). The parameters that fit both PPMS and particle rotation data are shown in Table I.

The magnitude of the Brownian dipole can be determined from a torque balance at critical frequencies, at which the Brownian dipole dominates the torque expression [Eq. (37)]. At frequencies <10 Hz, the Néel dipole component $\chi_N''(\omega_f)$ is estimated to be ≈ 0.02 rad (from the above-mentioned model) and at the critical frequency, the Brownian dipole phase lag $\theta_f - \theta_{1,B} = 90°$; hence m_B is the only unknown in Eq. (39). The Brownian dipole m_B and fractions f_B and f_N were determined in an iterative fashion by minimizing error in Eqs. (26)–(28) and Eq. (39). Explicitly, $f_B = m_B/\mathbf{m}$, where $\mathbf{m}$ is the total dipole in A m^2 by using χ_o for susceptibility in Eq. (20) and $f_N = 1 - f_B$, which is used to calculate $\chi_N''(\omega_f)$ in Eq. (27); then $\chi_N''(\omega_f)$ is used in Eq. (39). The values are shown in Table I. It is assumed that the magnitude of the Brownian dipole does not change significantly in this field and frequency range.

D. Brownian dynamics simulations

BD simulations were performed based on Eqs. (3) and (4) with an integration time of 0.01 ms, which is short enough to assume constant force but long enough for momentum relaxation [51]. Equation (3) can be approximated by using the midpoint rule to avoid calculating the gradient of the diffusion tensor [52–54]. Initial doublet, particle, and field orientation was always 0° or parallel to the x axis, with an initial separation of 3.03 μm, which is an estimate of the energy minimum at all frequencies determined from a probability distribution from experimental data. Simulations were run for at least 15 s, which was found to be sufficient to obtain particle and doublet average rotation frequency, and adequate given that doublets reach steady state after approximately <1 s. Particle coordinates (positions, angles) were recorded every 1 ms. Particle, wall, and solution properties used in the simulation are shown in Table I. The Néel phase lag values from the model [see Eqs. (26)–(28) and Table I] were directly used in BD simulations at 6 G.

Due to the particles' proximity to the underlying wall, translational motion parallel to the wall will be slowed [55]. However, translation-rotation coupling increases with wall proximity [44], speeding up translational motion. We made the assumption that the overall net effect of the wall would be a reduction in translational motion, although not as reduced as a single particle translating parallel to the wall. To validate this assumption, we ran Stokesian dynamics (SD) test cases that included particle-particle, particle-wall, and multibody hydrodynamics [44,54,56] and compared them to BD simulations run with a 1.35 resistance increase for the translational diagonal terms. The simulations agreed qualitatively near the critical frequency and at high frequencies. Regarding quantitative agreement, for ten trials at a high-frequency case (50 Hz at 6 G), the difference in mean doublet rotation for SD vs BD was ∼20% and the results were within one standard deviation of each other. For ten trials at a frequency right after the critical frequency (0.6 Hz at 6 G), the difference in mean doublet rotation was ∼30%. Since both the SD and BD results at these frequencies were still within the ranges that were observed in experiment, we used the computationally less expensive BD simulations.

IV. RESULTS AND DISCUSSION

A. Single particle rotation

Single particle rotation rates were measured in fields of 6 and 10 G and rotation frequencies from 0.1 to 100 Hz. Representative rotational trajectories are plotted in Fig. 5(a) from VM and BD simulations for particles in 0.8 and 80 Hz fields at 6 G. Oscillations in the angular trajectory at 0.8 Hz demonstrate that the particle cannot rotate as fast as the field, which occurs after a critical frequency. Figure 5(b) shows the fast Fourier transform (FFT) of the sine of the angular trajectories (normalized by the greatest nonzero peak)

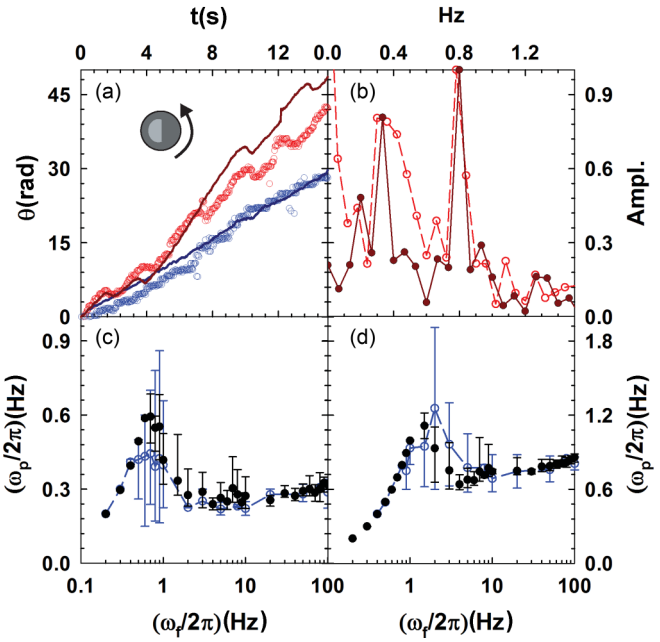

FIG. 5. (a) Angular trajectories of VM experiments and BD simulations of isolated single particles at 6 G and 0.8 Hz (red, top) and 80 Hz (blue, bottom) (see VM movies and BD renderings of particles rotating at 0.8 Hz in Video S1 [27]). In all plots, experimental results are shown by light, unfilled symbols, and the simulation results are shown by dark, filled symbols. (b) Fast Fourier transform (FFT) of the sine of the angular coordinate of the 0.8 Hz trajectories for both experiment and simulation. Single particle rotation frequency vs applied field frequency for (c) 6 G and (d) 10 G with experimental averages with range bars (min and max) and BD simulation results.

for both the simulation and experiment at 0.8 Hz. The BD simulation reproduces the single particle rotation, capturing both a dominant frequency at 0.8 Hz and a secondary frequency at ≈0.3 Hz.

Figures 5(c) and 5(d) summarize single particle rotation frequency vs field rotation frequency at 6 and 10 G for experiments and simulation. Particles rotate at the same frequency as the field up to critical frequencies of ≈0.6 Hz for 6 G and ≈1 Hz for 10 G. The results can be understood by considering the torques on both the Brownian and Néel dipoles. At low frequencies (<2 Hz for 6 G, <8 Hz for 10 G), the particles have an effectively "permanent" dipole, on the time scale of the experiment, which aligns with the field orientation via Brownian relaxation. At frequencies >2 Hz for 6 G and >8 Hz for 10 G, the field is rotating with a time scale on the order of ∼0.1 s, whereas the Brownian relaxation time is $\tau_B = 4\pi\eta\alpha^3/kT \approx 7.5$ s, and therefore the torque from the Brownian dipole averages zero.

Because the ensemble Néel dipole has a characteristic relaxation time of $\tau_N \approx 1 \times 10^{-9}$ s, it is aligned with the field at all frequencies. However, the Néel relaxation time distribution is broad (described by α), with a finite out-of-phase component of the Néel dipole [19], which produces a frequency-dependent torque on the particle [20,57]. As such, the particle rotation frequency plateaus, and then slightly increases as the phase lag begins to increase in external fields up to 100 Hz. It is expected that at frequencies >100 Hz, particle rotation will continue to increase as the out-of-phase component increases [19]. The agreement between simulations and experiments shows the dipole relaxation model accurately captures the measured dynamics. We proceed with these properties to analyze doublet rotation experiments.

B. Particles rotating within rotating doublets

We report in Fig. 6 the rotation of individual particles within doublets in 6 and 10 G fields from 0.1 to 100 Hz. Rotation frequency results were not significantly different from those of isolated rotating particles. The variation in particle rotation rates is most likely due to nonuniformity between particles, such as size, static susceptibility, and phase lag. To demonstrate the particle nonuniformity, Fig. 6(a) shows angular trajectories of particles rotating at 0.8 and 80 Hz at 6 G. The two experimental plots shown for the 0.8 Hz case are distinct particles rotating in the same doublet. For comparison, the isolated particle at 0.8 Hz in Fig. 5(a) rotates at a frequency in between these two particles.

Figure 6(b) shows the FFT of the sine of the angular trajectory of the faster particle in the doublet in Fig. 6(a).

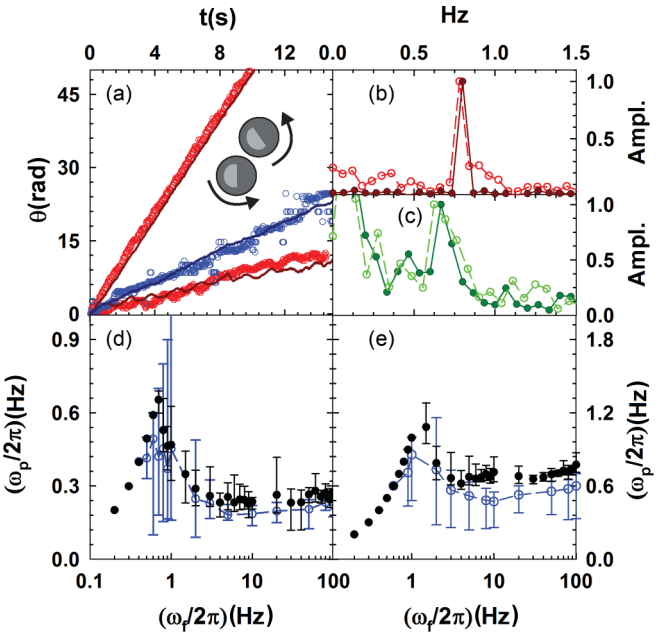

FIG. 6. (a) Angular trajectories of VM experiments and BD simulations of particles rotating within a doublet at 6 G and 0.8 Hz (red, top, and bottom) or 80 Hz (blue, middle) (see VM movies and BD renderings of particles rotating in a doublet at 0.8 and 80 Hz in Videos S2 and S3 [27]). The two 0.8 Hz experimental plots are of particles within the same doublet, illustrating the range in magnetic properties. In all plots, experimental results are shown by light, unfilled symbols, and the simulation results are shown by dark, filled symbols. (b) FFT of the sine of the angular coordinate of the faster 0.8 Hz trajectory for both experiment and simulation and (c) the FFT of the slower 0.8 Hz angular trajectory minus a linear fit of the same trajectory to capture the oscillation frequency of both experiment and simulation. Single particle rotation frequency within doublets vs applied field frequency for (d) 6 G and (e) 10 G with experimental averages with range bars (min and max) and BD simulation results.

The faster particle has a critical frequency greater than 0.8 Hz because it can still rotate with the field at 0.8 Hz, while its partner cannot. The slower particle is oscillating about an average rotation rate, indicating it is in a regime just past the critical frequency. BD simulations are fit to match the two particles' trajectories by increasing the Néel dipole phase lag for the faster particle, relative to the measured average (to increase torque), and decreasing the phase lag for the slower particle (to decrease torque). Figure 6(c) shows the FFT of the slower particle trajectory minus a linear fit to the average trajectory (which captures the secondary oscillation frequency) for both experiment and simulation in Fig. 6(a). The simulation captures the oscillation frequency in the experiment, as seen by the matching peaks at ≈0.67 Hz.

Figures 6(d) and 6(e) summarize particle rotation frequency within doublets vs the field rotation frequency for 6 and 10 G. The same general behavior is observed in these plots as isolated, single particles (Fig. 5). The particle follows the frequency of the field until a critical frequency of ≈0.6 Hz at 6 G. For 10 G experiments, the critical frequency is at ≈1 Hz, which is less than the ≈2 Hz simulation estimate. The discrepancy is most likely due to experimental oversampling of "slow" particles (i.e., particles with a smaller phase lag and/or smaller static susceptibility). Like the single particles, particles in a doublet continue to rotate even when the field frequency is several orders of magnitude greater than the Brownian relaxation time because the torque on the Néel dipole is nonzero. In the field frequency range 10–100 Hz, the particle frequency plateaus just above 0.2 and 0.5 Hz for 6 and 10 G, similar to the plateaus seen for single particles in Figs. 5(c) and 5(d).

The trajectory of the oscillating particle at 0.8 Hz is fit to a linear function to obtain an average rotation speed of 0.13 Hz. An available literature model [22] [Eqs. (40) and (41)] predicts the frequency of oscillations given the average particle rotation and the field frequency as 0.8 Hz–0.13 Hz = 0.67 Hz, which is close to the measured peak in Fig. 6(c). The critical frequency can also be estimated from this model, and is found to be ≈0.44 Hz, which is lower than the average measured value [see Fig. 6(d)]. This also confirms what has been observed experimentally for this unique particle; it has a smaller overall susceptibility, Brownian dipole, and/or a smaller Néel dipole phase lag with the field, decreasing the field torque and reducing the critical frequency.

The effect of unique particle properties is evidenced by the large variation in particle rotation in the frequency regime near the critical frequency, as shown in Figs. 5(c), 5(d), 6(d), and 6(e). As expressed in Eq. (39), the Brownian dipole m_B and the out-of-phase Néel susceptibility $\chi_N''(\omega_f)$ impact rotation at the lower frequencies and near the critical frequency, while $\chi_N''(\omega_f)$ influences high-frequency rotation. Changing the Néel dipole phase lag by ∼0.01 rad will shift the critical frequency for unique single particles. It has been noted previously for these particles that nonuniformity can alter the observed dynamics [21]; thus the stochastic nature of the system, including particle heterogeneity, explains why in some cases the simulation data are not within range of the experimental data. The parameters presented in Table I reproduce with good agreement the features observed in the single particle and particle in doublet experiments, but can be tuned to obtain more quantitative agreement for distinct particles.

C. Doublet rotation

Figure 7 displays representative measured and simulated doublet rotational trajectories for doublets experiencing a 0.8 or 80 Hz field at 6 G. Oscillations in the 0.8 Hz trajectories indicate this frequency is greater than the critical frequency for doublets. The normalized FFT plots of the sine of the 0.8 Hz experiment and simulation trajectories in Fig. 7(b) show alignment of the peaks at ≈0.3 Hz, demonstrating that the simulation captures the dominant doublet frequency. The FFT of the 0.8 Hz trajectories minus linear fits is shown in Fig. 7(c) to obtain the frequency of the rotational oscillations. The experiment data have two peaks at ≈0.8 and ≈1 Hz, most likely due to particle nonuniformity, whereas the simulation shows a single oscillation frequency at ≈1 Hz.

Oscillations in doublet rotation occur just past the observed critical frequency because the dipoles of two particles rotate faster than the doublet vector. When the angle between the

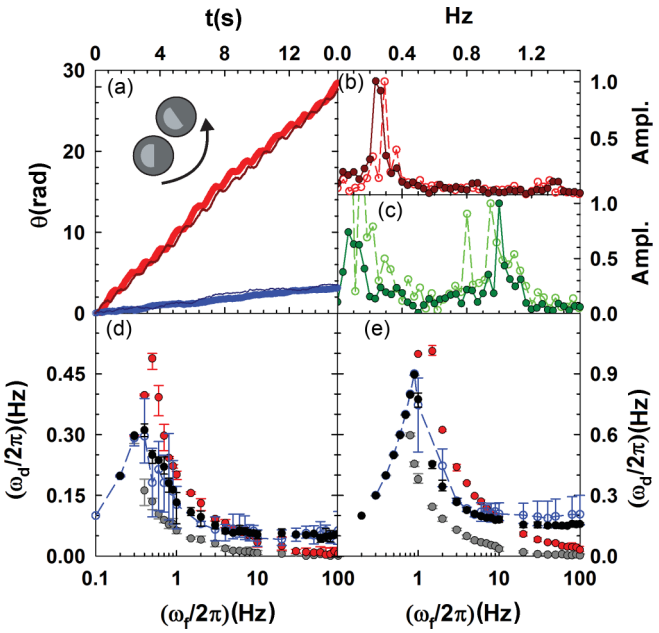

FIG. 7. (a) Angular trajectories of VM experiments and simulations of doublets rotating at 6 G and 0.8 Hz (red, top) or 80 Hz (blue, bottom) (see VM movies and BD renderings of rotating doublets at 0.8 and 80 Hz in Videos S2 and S3 [27]). In all plots, experimental results are shown by light, unfilled symbols, and the simulation results are shown by dark, filled symbols. (b) FFT of the sine of the angular coordinate of the 0.8 Hz trajectory for both experiment and simulation and (c) the FFT of the 0.8 Hz angular trajectory minus a linear fit of the respective trajectory to capture the oscillation frequency for both experiment and simulation. Doublet rotation frequency vs applied field frequency for (d) 6 G and (e) 10 G with experimental averages with range bars (min and max) and BD simulation results. In plots (d,e), simulations with the exact mobility matrix [Eq. (30)] (black) are compared to simulations run as if the particles are noninteracting with all off-diagonal elements in the matrix zero (red) and as if the particles have no translation-rotation or rotation-translation coupling [i.e., $\mathbf{b}$, $\tilde{\mathbf{b}}$ in Eq. (30) are zero] (gray).

doublet vector and the weighted average dipole (i.e., Néel and Brownian) reaches 90°, the doublet vector rotates backward to realign with the particle dipoles, and the cycle begins again. The previously mentioned model for single particle rotation, which relates the critical frequency and oscillation frequency to the average rotation frequency for a given field frequency, is adapted from a one-dimensional torque balance of a bound doublet [22]. Such a simple torque balance may not easily capture the doublet rotation rate, because (1) the doublet may not be rigidly rotating, (2) the doublet vector is coupled to a torque balance involving the individual particle dipoles, and (3) the dipoles experience stochastic translation and rotation that may not be captured by a simple average interaction.

We compare the simple model to the doublet rotational trajectory at 0.8 Hz to determine how the model's assumptions may limit its applicability for quantitative predictions of freely rotating doublets. First, we estimate that the overall dipoles rotate at the same frequency as the field at 0.8 Hz; this should be a valid assumption given the relaxation time of the Néel dipole and the fact that the Brownian dipole is an order of magnitude smaller than the Néel dipole (see Table I). Then, given the average doublet rotation rate of 0.3 Hz, the oscillation frequency should be 2(0.8 Hz–0.3 Hz) = 1 Hz [see Eq. (43)]. This is comparable to the observed peak in Fig. 7(c) for the simulation, but the secondary peak at 0.8 Hz for the experiment may indicate that the dipoles are not rotating at the same rate as the field. Next, using the value of 0.8 Hz as the dipole rotation, the estimate of the critical frequency can also be calculated from the model, and for this doublet it is ≈0.6 Hz, which is higher than the experimental upper bound of 0.4 Hz [see Fig. 7(d)]. We attribute this discrepancy to the fact that the doublet is not rigidly rotating.

Figures 7(d) and 7(e) summarize doublet frequency vs field frequency at 6 and 10 G. BD simulations with the exact particle-particle hydrodynamic tensor [Eq. (30) with all terms] are plotted as dark circles and fall within the upper and lower values observed in the experiments. Critical frequencies are observed at 0.4 Hz for 6 G and 1 Hz for 10 G. Low-frequency rotation below the critical frequency can be understood as follows: The particles' Brownian and Néel dipoles rotate at the same frequency as the field, and as a result, the doublet also rotates due to the favorable head-to-tail alignment of their dipoles. This is captured in Eq. (16) where particles experience a tangential force in the θ_r direction when their dipoles are not aligned along the center-to-center vector $\mathbf{r}$. At intermediate frequencies just above the critical frequency, the doublet vector increasingly lags behind the particle dipoles and when the lag reaches 90°, the doublet rotates backwards (hence the observed oscillations in the angular trajectory) to realign with the dipoles. As described earlier, at higher frequencies, the Brownian dipole torque averages out to zero but the Néel dipoles of the particles are still rotating with the field (with a characteristic lag). In this regime, the particles cannot reorient around each other, on the time scale of the field rotation, to align their Néel dipoles as part of doublet rotation. This would imply that the doublet would not rotate at frequencies much greater than the critical frequency for doublets due to viscous drag. However, doublets are observed to continue to rotate at high frequencies in VM experiments (see VM movie at 80 Hz in Video S3 of the Supplemental Material [27]).

The significance of hydrodynamic interactions and their contribution to doublet rotation is illustrated by testing two additional approximate mobility matrices in the BD simulations, which are also shown in Figs. 7(d) and 7(e). One approximation is a mobility matrix with only diagonal terms corresponding to $a_{ii} = 1/6\pi\eta a$ and $c_{ii} = 1/8\pi\eta a^3$ [red points in Figs. 7(d) and 7(e) shifted to the right of the critical frequency]. These simulations overestimate the critical frequency because the particles experience an overall smaller viscous resistance. In addition, doublet rotation vanishes at high frequencies in simulations with only diagonal terms. These results imply that the doublet rotates at low frequencies due to dipolar interactions, a behavior that is still qualitatively captured by the simple hydrodynamic model, and at high frequencies due to hydrodynamic interactions that are not captured by this model. It appears that rotation of the particles within the doublet couples to their translation [$\mathbf{b}, \tilde{\mathbf{b}}$ in Eq. (30)], leading to overall doublet rotation at high frequencies.

To test the role of translation-rotation, BD simulations were also performed with $\mathbf{b}$ and $\tilde{\mathbf{b}}$ removed from the mobility matrix; the results are shown as gray points (shifted to the left of the critical frequency) in Figs. 7(d) and 7(e). In this case, the doublet rotation rate is underestimated for frequencies >0.3 Hz for 6 G and >0.7 Hz for 10 G, indicating that translation-rotation coupling contributes to doublet rotation even at low frequencies. At higher field frequencies, doublet rotation vanishes without including coupling, which indicates that the translation-rotation coupling is the sole mechanism causing doublet rotation in this regime. This effect would still occur in simulations that only include far field hydrodynamics, although to a lesser extent, because the coupling terms in Eq. (32) remain qualitatively unchanged.

The results highlight the connection between individual particle dynamics and doublet dynamics: The particles' rotation within the doublet produces an asymmetric flow, causing particles to translate around each other and the doublet to rotate. This finding is supported by another literature study that also showed individual particle rotation contributed to rotation of larger clusters via a translation-rotation coupling mechanism [32]. Due to the relationship between particles and doublet rotation, the doublet experimental results can be used to confirm the dipole relaxation model applied in BD. At 10 G, slightly greater Néel phase lag values (+∼0.01 rad) than those from the model fit parameters [α and τ_N in Eqs. (26)–(28)] were found to better match single particle and doublet experiments, but follow the trend of the model.

D. Particle separation dynamics

Particles in rotating doublets experience varying degrees of fluctuations in their center-to-center distance, $r = |\mathbf{r}|$ with varying field frequency. Separation distance as a function of time is plotted in Fig. 8 for three representative frequency ranges at 6 and 10 G. At frequencies below the critical frequency [Figs. 8(a) and 8(d)], the dipoles are aligned with $\mathbf{r}$, and the dipole-dipole interaction is the same as if the field were constant. As such, strong dipolar attraction holds particles together with minimal fluctuations in r. At field rotation frequencies much greater than the critical frequency [Figs. 8(c) and 8(f)], the Néel dipole is rotating several orders

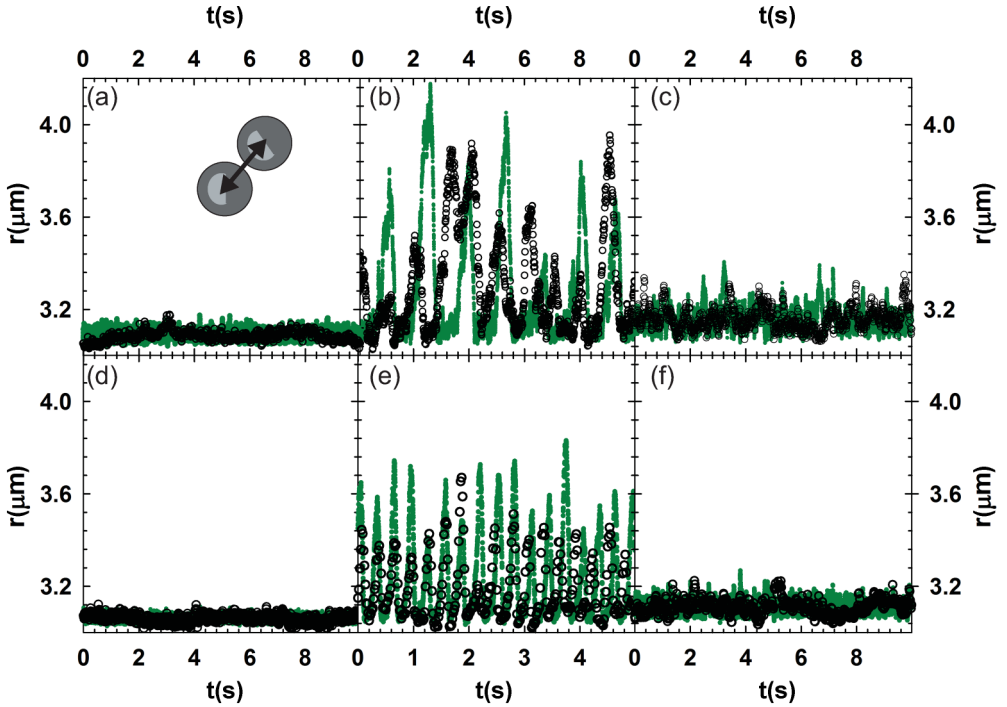

FIG. 8. Representative plots of particle-particle separation, r, vs time, t, at 6 G (a–c) and 10 G (d–f) at frequencies below the critical frequency [(a,d) 0.1 Hz], just after the critical frequency [(b) 0.6, (d) 2 Hz], and two orders of magnitude higher than the critical frequency [(c) 50 Hz, (f)100 Hz] for experiments (black, open circles) and simulations (green, closed circles). Oscillations in r are observed at frequencies near 0.5 Hz for 6 G and near 2 Hz for 10 G (similar to frequencies where secondary angular oscillations are seen for single particles and doublets in Figs. 5–7).

of magnitude faster than **r** such that the average angle between **r** and the dipoles is assumed to be ≈45°. This still corresponds to a net attraction between particles [Eq. (16)], although it is much weaker than aligned dipoles at 0°, thus producing slightly larger fluctuations in r compared to the low-frequency limit.

For field rotation frequencies near the critical frequency [Figs. 8(b) and 8(e)], the particles intermittently separate and come back together at the same frequency as the oscillations in the doublet rotation (see Fig. 7). The simultaneous oscillations in θ_r (Fig. 7) and r (Fig. 8) are observable in both experiment and simulations (see a representative VM experiment and BD simulation of a doublet at 0.8 Hz in Video S2 [27]). In this regime, the angle between the single particle dipoles and the doublet vector is periodically between 55° and 90° and the particles experience a temporary repulsion. For comparison, the angular transition from attraction to repulsion occurs at ≈55° by solving a simplified version of Eq. (16) for point dipoles with identical magnitude restricted to the x-y plane. The temporary repulsion causes the particles to separate at the same time as the temporary reversal in rotation direction when the relative angle reaches 90°.

The BD simulation results in Fig. 8 capture the observed r oscillations at 0.6 and 2 Hz for 6 and 10 G, as well as the Brownian fluctuations in r in the low- and high-frequency ranges below and above the transition frequency range. The dipolar attraction is strongest when the angle between the single particle dipoles and doublet vector is ≈0°, which is the case at 0.1 Hz where the variation in r is seen to be ≈100 nm. The dipolar attraction between particles decreases at 50–100 Hz, as shown by the ≈200 nm variation in r at these frequencies. Variation in r is slightly greater in the simulation than is observed experimentally (observed in histograms of r), and this discrepancy is most pronounced in the oscillation regime. The error is most likely due to the approximate point-dipole potential [i.e., Eq. (16)] used in simulations, which at close range overestimates the repulsion by ∼10% when the dipoles are perpendicular to the doublet vector and underestimates the attraction for aligned dipoles by ∼20% [58].

V. CONCLUSIONS

Our findings demonstrate agreement between experiments, simulations, and models of superparamagnetic particle dynamics in rotating magnetic fields for single particles and doublets. Rotation of particles and doublets depends on dipole-field interactions, dipole-dipole interactions, and hydrodynamic interactions. Our results show that both dipolar interactions (including relaxation mechanisms) and hydrodynamic interactions (including exact two-body, translation-rotation coupling) play an essential role in capturing nonequilibrium, steady-state rotation of magnetic particles vs field rotation frequency. Simulations and modeling results verify that single particle rotation within doublets directly affects overall doublet rotation (via hydrodynamics), which we show is essential for qualitatively and quantitatively matching experiments with simulations. The effect is most notable at high frequencies when an increased Néel phase lag causes the particles to continue rotating. The direct measurements and rigorous models developed for single

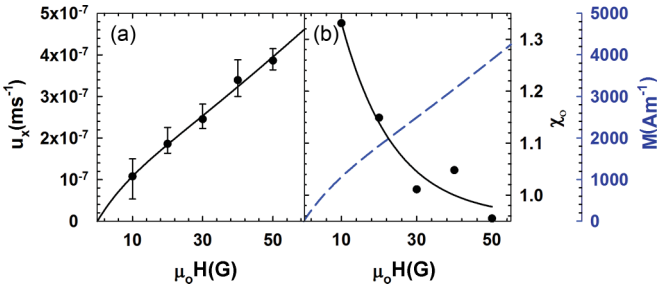

FIG. 9. (a) Measured mean drift, u_x, (points) vs field strength, $\mu_o H$, in gauss. The bars are max and min values. (b) Susceptibility, χ_o, (points) vs $\mu_o H$ computed from Eq. (A4) and fit to the empirical function in Eq. (A5) (solid line). The solid line in (a) is obtained by inserting Eq. (A5) for the value of $\chi_o(H)$ in Eq. (A4) and solving for u_x. Magnetization, $M = \chi_o(H)H$, is also plotted in (b) (dashed line) and agrees qualitatively with previously reported magnetization curves for superparamagnetic particles [60].

particles and rotating particle pairs within doublets provide a foundation to understand interactions and dynamics of magnetic particles in time varying fields important to colloidal assembly in field-driven systems.

ACKNOWLEDGMENTS

We acknowledge financial support provided by the National Science Foundation (Grant No. CBET-1234981). We thank Dr. Robert Leheny for the use of the magnetic quadrupole and Dr. Tyrel McQueen for use of the PPMS.

APPENDIX: MEASURING STATIC SUSCEPTIBILITY

The effective static susceptibility, χ_o, for the particles is reported by the manufacturer as 0.96, but to obtain an estimate at the order of the field intensities used in this work, magnetophoresis experiments were conducted with a 5 G/mm gradient at several field intensities. Single particle drift **u** is measured using particle tracking, and measurements are shown in Fig. 9(a). The susceptibility is calculated by solving a force balance between the magnetophoretic force [59] and viscous drag as

$$\mathbf{F}_{\text{mag}} = (4/3)\pi a^3 \chi_o(H)\mu_o H \nabla \mathbf{H}, \tag{A1}$$

$$\mathbf{F}_{\text{drag}} = 6\pi\eta a f(h)\mathbf{u}, \tag{A2}$$

where $f(h) = 2.8$ is a hydrodynamic correction due to lateral movement at height h from the wall [54,61], and h is estimated from a balance of gravity and electrostatic repulsion as [62]

$$h = \kappa^{-1} \ln[\kappa B^{pw}/G]. \tag{A3}$$

By equating Eqs. (A1) and (A2) at steady state, the susceptibility as a function of field strength, where the field gradient and the drift are in the x direction, is as shown:

$$\chi_o(H) = \frac{(4/3)\pi a^3 \mu_o H \nabla H_x}{6\pi\eta a f(h) u_x}. \tag{A4}$$

We conducted six trials at 10 G, and three trials for all other field intensities. The results are fit to an empirical function that has the form

$$\chi_o(H) = c_1 + c_2 \exp(-c_3 \mu_o H), \tag{A5}$$

where $c_1 = 0.9569$, $c_2 = 0.7709$, and $c_3 = 0.072$. Experiments are not conducted at 6 G due to the need to run very long videos to get an accurate drift. Instead, $\chi_o(6G/\mu_o)$ was determined based on Eq. (A5). Magnetization defined as $M = \chi_o(H)H$ is plotted on a separate y axis in Fig. 9(b). Note that throughout the main text, the H in $\chi_o(H)$ is dropped and χ_o is referred to as the static susceptibility.

[1] C. E. Sing, L. Schmid, M. F. Schneider, T. Franke, and A. Alexander-Katz, Proc. Natl. Acad. Sci. U. S. A. **107**, 535 (2010).
[2] S. Y. Park, H. Handa, and A. Sandhu, Nano Lett. **10**, 446 (2010).
[3] S. Bleil, D. W. M. Marr, and C. Bechinger, Appl. Phys. Lett. **88**, 263515 (2006).
[4] T. O. Tasci, P. S. Herson, K. B. Neeves, and D. W. M. Marr, Nat. Commun. **7**, 10225 (2016).
[5] J. de Vicente, D. J. Klingenberg, and R. Hidalgo-Alvarez, Soft Matter **7**, 3701 (2011).
[6] A. Weddemann, F. Wittbracht, B. Eickenberg, and A. Hütten, Langmuir **26**, 19225 (2010).
[7] J. Yan, M. Bloom, S. C. Bae, E. Luijten, and S. Granick, Nature (London) **491**, 578 (2012).
[8] D. Du, D. Li, M. Thakur, and S. L. Biswal, Soft Matter **9**, 6867 (2013).
[9] J. Yan, S. C. Bae, and S. Granick, Soft Matter **11**, 147 (2015).
[10] J. W. Swan *et al.*, Proc. Natl. Acad. Sci. U. S. A. **109**, 16023 (2012).
[11] S. Melle, G. G. Fuller, and M. A. Rubio, Phys. Rev. E **61**, 4111 (2000).
[12] I. Petousis, E. Homburg, R. Derks, and A. Dietzel, Lab Chip **7**, 1746 (2007).
[13] S. Krishnamurthy, A. Yadav, P. E. Phelan, R. Calhoun, A. K. Vuppu, A. A. Garcia, and M. A. Hayes, Microfluid. Nanofluid. **5**, 33 (2008).
[14] Y. Gao, M. A. Hulsen, T. G. Kang, and J. M. J. den Toonder, Phys. Rev. E **86**, 041503 (2012).
[15] S. Melle, O. G. Calderón, G. G. Fuller, and M. A. Rubio, J. Colloid Interface Sci. **247**, 200 (2002).
[16] J. Dobnikar, A. Snezhko, and A. Yethiraj, Soft Matter **9**, 3693 (2013).
[17] E. M. James and S. Alexey, Rep. Prog. Phys. **76**, 126601 (2013).
[18] A. van Reenen, A. M. de Jong, and M. W. J. Prins, Lab Chip **15**, 2864 (2015).
[19] X. J. A. Janssen, A. J. Schellekens, K. van Ommering, L. J. van Ijzendoorn, and M. W. J. Prins, Biosens. Bioelectron. **24**, 1937 (2009).
[20] B. H. Erné, M. Claesson, S. Sacanna, M. Klokkenburg, E. Bakelaar, and B. W. M. Kuipers, J. Magn. Magn. Mater. **311**, 145 (2007).

[21] M. M. van Oene, L. E. Dickinson, F. Pedaci, M. Köber, D. Dulin, J. Lipfert, and N. H. Dekker, Phys. Rev. Lett. **114**, 218301 (2015).
[22] G. Helgesen, P. Pieranski, and A. T. Skjeltorp, Phys. Rev. A **42**, 7271 (1990).
[23] P. Dominguez-Garcia, S. Melle, O. Calderon, and M. A. Rubio, Colloids Surf., A **270-271**, 270 (2005).
[24] B. E. Kashevsky and V. A. Kuzmin, J. Phys. D **29**, 2579 (1996).
[25] K. Takamura, H. L. Goldsmith, and S. G. Mason, J. Colloid Interface Sci. **72**, 385 (1979).
[26] D. Velegol, S. Catana, J. L. Anderson, and S. Garoff, Phys. Rev. Lett. **83**, 1243 (1999).
[27] See Supplemental Material at http://link.aps.org/supplemental/10.1103/PhysRevE.94.042613 for videos of VM experiments and BD simulations for the conditions reported in the captions of Figs. 1 and 5–7.
[28] T. G. Kang, Y. Gao, M. A. Hulsen, J. M. J. den Toonder, and P. D. Anderson, Comput. Fluids **86**, 569 (2013).
[29] R. Soheilian, Y. S. Choi, A. E. David, H. Abdi, C. E. Maloney, and R. M. Erb, Langmuir **31**, 8267 (2015).
[30] P. Tierno, R. Muruganathan, and T. M. Fischer, Phys. Rev. Lett. **98**, 028301 (2007).
[31] A. Ranzoni, X. J. A. Janssen, M. Ovsyanko, L. J. van Ijzendoorn, and M. W. J. Prins, Lab Chip **10**, 179 (2010).
[32] S. Jäger, H. Stark, and S. H. L. Klapp, J. Phys.: Condens. Matter **25**, 195104 (2013).
[33] D. J. Jeffrey and Y. Onishi, J. Fluid Mech. **139**, 261 (1984).
[34] E. Dickinson, S. A. Allison, and J. A. McCammon, J. Chem. Soc., Faraday Trans. 2 **81**, 591 (1985).
[35] D. J. Beltran-Villegas, B. A. Schultz, N. H. P. Nguyen, S. C. Glotzer, and R. G. Larson, Soft Matter **10**, 4593 (2014).
[36] W. B. Russel, D. A. Saville, and W. R. Schowalter, *Colloidal Dispersions* (Cambridge University Press, New York, 1989).
[37] J. D. Jackson, *Classical Electrodynamics*, 3rd ed. (John Wiley & Sons, New York, 1998).
[38] S. L. Biswal and A. P. Gast, Phys. Rev. E **69**, 041406 (2004).
[39] K. S. Cole and R. H. Cole, J. Chem. Phys. **9**, 341 (1941).
[40] P. C. Fannin, B. K. P. Scaife, and S. W. Charles, J. Magn. Magn. Mater. **72**, 95 (1988).
[41] W. F. Brown, Jr., Phys. Rev. **130**, 1677 (1963).
[42] P. C. Fannin, L. Cohen-Tannoudji, E. Bertrand, A. T. Giannitsis, C. Mac Oireachtaigh, and J. Bibette, J. Magn. Magn. Mater. **303**, 147 (2006).
[43] J. Liu and R. G. Larson, J. Chem. Phys. **138**, 174904 (2013).
[44] J. W. Swan and J. F. Brady, Phys. Fluids **19**, 113306 (2007).
[45] M. H. Lee, C. P. Lapointe, D. H. Reich, K. J. Stebe, and R. L. Leheny, Langmuir **25**, 7976 (2009).
[46] J. Santana-Solano, D. T. Wu, and D. W. M. Marr, Langmuir **22**, 5932 (2006).
[47] S. M. Anthony, M. Kim, and S. Granick, Langmuir **24**, 6557 (2008).
[48] A. Wittmeier, A. Leeth Holterhoff, J. Johnson, and J. G. Gibbs, Langmuir **31**, 10402 (2015).
[49] J. C. Crocker and D. G. Grier, J. Colloid Interface Sci. **179**, 298 (1996).
[50] J. Lim, C. Lanni, E. R. Evarts, F. Lanni, R. D. Tilton, and S. A. Majetich, ACS Nano **5**, 217 (2011).
[51] D. L. Ermak and J. A. McCammon, J. Chem. Phys. **69**, 1352 (1978).
[52] M. Fixman, J. Chem. Phys. **69**, 1527 (1978).
[53] P. S. Grassia, E. J. Hinch, and L. C. Nitsche, J. Fluid Mech. **282**, 373 (1995).
[54] S. Anekal and M. A. Bevan, J. Chem. Phys. **122**, 034903 (2005).
[55] H. Brenner, Chem. Eng. Sci. **16**, 242 (1961).
[56] S. Anekal and M. A. Bevan, J. Chem. Phys. **125**, 034906 (2006).
[57] S. B. Trisnanto and Y. Kitamoto, Phys. Rev. E **90**, 032306 (2014).
[58] D. Du, F. Toffoletto, and S. L. Biswal, Phys. Rev. E **89**, 043306 (2014).
[59] D. Fleisch, *A Student's Guide to Maxwell's Equations* (Cambridge University Press, Cambridge, 2008).
[60] G. Fonnum, C. Johansson, A. Molteberg, S. Mørup, and E. Aksnes, J. Magn. Magn. Mater. **293**, 41 (2005).
[61] A. J. Goldman, R. G. Cox, and H. Brenner, Chem. Eng. Sci. **22**, 637 (1967).
[62] D. C. Prieve and N. A. Frej, Langmuir **6**, 396 (1990).